Check for updates

Thermodynamic and kinetic properties of layered-CaCo$_2$O$_4$ for the Ca-ion batteries: a systematic first-principles study†

Haesun Park [ID] *[ab] and Peter Zapol [ID] *[ab]

One of the more promising directions in multivalent energy storage is systems based on Ca ion intercalation due to the potential for high voltage and capacity. A major challenge for enabling such a battery is to find cathode materials capable of fast ionic diffusion and reversible insertion of Ca ions. Here, on the basis of first-principles calculations, we have demonstrated that layered CaCo$_2$O$_4$ exhibits favorable thermodynamic and kinetic properties that should enable topotactic Ca ion intercalation reactions. The P3-type layered Ca$_x$Co$_2$O$_4$ ($0 < x < 1$) with either of space groups of $P1$ or $P2_1/m$ are stable at multiple Ca concentrations and show a smooth voltage plateau higher than 3 V up to $X = 0.5$. The energy barriers of the single Ca ion migration are as low as 0.36 eV and 0.27 eV at the dilute and high vacancy concentration limits, respectively. Although varying the vacancy environments of the diffusing atom influences the migration barriers, they do not exceed 0.6 eV. Stochastic analysis of Ca hopping events performed by *ab initio* molecular dynamics (AIMD) simulation has shown that the migration barriers are lower than 0.32 eV. Therefore, the Ca diffusivity at room temperature extrapolated from the AIMD results is comparable to Li diffusivity ($>10^{-10}$ cm^{2}s^{-1}) in conventional Li cathode materials, suggesting the feasibility of layered Ca$_x$Co$_2$O$_4$ as multivalent cathode materials. Finally, the structural factors that enable fast diffusion are discussed.

Introduction

Calcium-based rechargeable batteries are a promising niche replacement for energy storage chemistries based on Li chemistry mainly due to the relative abundance of necessary raw materials in the Earth's crust (Li: 0.0007%, Ca: 5%) and its concomitant potential of low cost and stable supply chain.[3] In addition to availability, the multivalency of Ca enables superior charge density compared to monovalent ions since the number of Ca ions in the redox reaction is only half for the same charge. While the Mg-ion counterpart also possesses similar advantages, which have led to very intensive research over the past decade for utilizing Mg ion for intercalation batteries, little effort, by comparison, has been applied to Ca-ion systems.[4]

Despite the potential benefits of Ca-ion chemistry surpassing Mg-ion, there has been little attention focused on rechargeable Ca-ion batteries.[5] Besides the advantages noted above, as the strandard electrode potential of Ca is 500 mV lower than that of Mg,[6] we can expect higher battery voltage and corresponding higher energy density. In addition, the larger ionic radius of Ca (114 pm) when compared to Mg (84 pm)[7] entails less polarization which is beneficial to diffusivity of ions in a liquid electrolyte.[8] However, there are limited examples of cathode materials that can reversibly store Ca-ions[9–12,73,74] and their electrochemical performance (*e.g.* cell voltage, cyclability) is required to demonstrate the potential of Ca-ion batteries. Although electrolytes capable of plating/stripping the Ca-ion[13–16] and the system co-intercalating Ca solvation shell into the graphite[17,18] were recently reported, cathode materials utilizing lattice Ca for entailing high voltage and capacity are yet to be discovered that fulfill promises for Ca-ion based energy storage devices.

Considering the widely used cathode materials as a starting point in the search for new Ca-ion materials, layered inorganic compounds should be able to serve as hosts for Ca ion, given that Li, Na, and K can reversibly intercalate into this type of materials. The ionic radius of Ca (114 pm) is smaller than those of Na (116 pm) and K (152 pm),[7] and so we can speculate that the host materials (de)intercalating Na or K can do Ca as well. The most widely used and well-studied materials that can electrochemically (de)intercalate the alkali cations are materials based on the layered LiCoO$_2$ compound.[19] In addition to Li, there are reports that the layered CoO$_2$ can be used as a cathode material for Na- and K-ion based energy storage as well.[20–23] However, layered CoO$_2$ was excluded from consideration as

[a]Materials Science Division, Argonne National Laboratory, 9700 S Cass Ave, Lemont, IL 60439, USA. E-mail: parkh@anl.gov; zapol@anl.gov

[b]Joint Center for Energy Storage Research (JCESR), Argonne National Laboratory, 9700 S Cass Ave, Lemont, IL 60439, USA

† Electronic supplementary information (ESI) available. See DOI: 10.1039/d0ta07573f

21700 | *J. Mater. Chem. A*, 2020, **8**, 21700–21710

This journal is © The Royal Society of Chemistry 2020

a cathode for Mg intercalation because $MgCo_2O_4$ prefers the spinel structure,[24] and its ionic mobility is not sufficient (Mg migration barrier, $E_a = \sim 700$ meV) to pursue further exploration.[25] It was also shown that this material decomposes rather than deintercalates Mg upon charging.[26]

In contrast, we can infer from its reported thermodynamic and kinetic properties that the layered $CaCo_2O_4$ is suitable for Ca-ion cathode. Cushing *et al.* reported that the P2 or P3 type layered $Ca_xCo_2O_4$ can be stabilized at a variety of Ca concentrations x including 0.52, 0.54, 0.70, and 1.[27] The facile synthesis was enabled by mixing the $Na_{2x}Co_2O_4$ precursor with anhydrous $(x + 0.1)Ca(NO_3)_2$ to prompt ion exchange between Na and Ca, and this synthesis procedure was reproduced by multiple studies.[28,29] This observation manifests that the removal of Ca up to ~ 0.5 from layered-$CaCo_2O_4$ is not susceptible to chemical decomposition and we can utilize this chemical range as a topotactic Ca intercalation reaction. Another critical property of being a promising cathode material is the fast kinetics of cations within the host material. The fact that the $Ca_xCo_2O_4$ ($x <$ 1.0) can be only synthesized by ion exchange, but not by solid-state reaction[27] makes this material more intriguing for Ca intercalating cathode. The facile ion exchange between Na and Ca in the layered-CoO_2 frameworks signifies that Ca can readily diffuse along the plane between CoO_2 layers. Putting these experimentally observed various compositions of $Ca_xCo_2O_4$ and the diffusion behaviour of Ca, $CaCo_2O_4$ can be a noteworthy candidate for Ca intercalating cathode. To the best of our knowledge, there is one case that successfully charge and discharge $CaCo_2O_4$ cathode using the V_2O_5 as an anode.[2]

In the present study, we demonstrate that the calculated thermodynamic and kinetic properties of layered $CaCo_2O_4$ are favorable for the facile Ca intercalation reaction which can be exploited as cathode in Ca-ion batteries. We used P3-type layered $CaCo_2O_4$ polymorphs with space groups of $P1$ and $P2_1/m$ as model structures. From the calculated equilibrium phase diagram, we found that the various Ca deintercalated $Ca_xCo_2O_4$ ($0.5 < x < 1.0$) are thermodynamically stable in either $P1$ or $P2_1/m$ structure. From the phase diagram with the assumption that metastable layered-CoO_2 is a ground state, additionally, $Ca_{0.25}Co_2O_4$ is stable. The corresponding voltage profile is relatively flat up to $Ca_{0.5}Co_2O_4$. Also, the reaction reinserting Ca into layered CoO_2 prefers to produce layered-$CaCo_2O_4$ over competing conversion to binaries/ternaries, signifying that topotactic Ca intercalation reaction is thermodynamically favorable. The Ca diffusion in the layered-CoO_2 is calculated to be fast at both high and dilute vacancy limits. The energy barriers of single ionic hopping through the low energy inter-zigzag mechanism were calculated to be 0.36 eV and 0.42 eV at dilute limit for $P1$ and $P2_1/m$, respectively. The barriers at high vacancy limit were as low as 0.27 eV for both structures. Near the dilute vacancy limit concentration, varying the local vacancy environments of diffusing atom alters the Ca-ion migration barrier, but the energy barrier remains less than 0.6 eV for the inter-zigzag mechanism. We also performed *ab initio* molecular dynamics (AIMD) simulations to stochastically sample the Ca-ion migration events in order not to overlook the effect of cooperative migrations. The Ca-ion migration barriers in the nominal composition of $Ca_{0.5}Co_2O_4$

estimated from the Arrhenius equation were 0.19 eV and 0.32 eV for $P1$ and $P2_1/m$ structures, respectively. The extrapolated diffusivities of Ca-ion at room temperature were comparable to those of Li in conventional cathodes.

Method

First-principles calculations on the basis of the density functional theory (DFT)[30] were performed as implemented in the Vienna *ab initio* simulation package (VASP).[31] The core–valence electron interactions are described by the projector-augmented wave (PAW)[32,33] potentials and the plane-wave cutoff energy was set to 520 eV which meets the standard convergence criteria of 1 meV per atom (Fig. S1†). The exchange–correlation functional takes the generalized gradient approximation (GGA) formulation suggested by Perdew–Burke–Ernzerhof (PBE).[34] The delocalization of the unpaired d-electron in the transition metals species, Co, was amended by adding a Hubbard U correction (U = 3.32 eV)[35] because of its accurate prediction of formation enthalpies of compounds involving Co[35,36] and the average intercalation voltage of $LiCoO_2$ layered cathode.[37] The spin-polarized calculations with initial state of unpaired electrons set to ferromagnetic ordering were performed unless otherwise stated. For Co^{3+} ions, initial low spin configurations were adopted. The k-point meshes were generated using the Python Materials Genomics (pymatgen) code,[38] with a density of at least 1000/atom unless otherwise stated. This k-point density has been used extensively in calculations of oxide systems, which were generally converged to the standard criteria (1 meV per atom).[2] Convergence tests for our systems, $P1$- and $P2_1/m$-$CaCo_2O_4$, also confirm that a density of 1000/atom is sufficient as shown in Fig. S1.†

The symmetry inequivalent structures of $Ca_xCo_2O_4$ ($0 < x < 1$) are constructed using the Clusters Approach to Statistical Mechanics (CASM) package[39] and they are fully relaxed to the atomic force tolerance of 0.02 eV Å^{-1}. The Ca–Co–O ternary phase diagram was calculated using the pymatgen code. The formation energies of layered $Ca_xCo_2O_4$ with intermediate Ca-ion content were calculated with the relative energy references of charged and discharged phases. Here, for the charged phase, we assume that the layered CoO_2 is the ground state. From the formation energy convex hull, we evaluate the piecewise voltage profile by calculating the equilibrium voltage between neighbouring stable intermediate phases.

The climbing image nudged elastic band (NEB)[40] method was adopted to evaluate the single ionic migration of Ca-ion in the layered structure. The simulation cells for NEB consisted of a supercell constructed from a $2 \times 2 \times 2$ replication of the $CaCo_2O_4$ unit cell to avoid the fictitious interactions among diffusing atoms in the periodic images. The NEB calculations were relaxed to the atomic force tolerance of 0.05 eV Å^{-1}. The NEB calculations are performed with GGA-PBE functional because the metastability of the electronic structure at the intermediate images entangles the convergence of NEB calculations[25] and there is no evidence that the inclusion of Hubbard correction can improve the accuracy of NEB.[41–44] To describe the contribution of van der Waals interactions at the high vacancy

This journal is © The Royal Society of Chemistry 2020

J. Mater. Chem. A, 2020, **8**, 21700–21710 | **21701**

limit accurately, we adopted strongly constrained and appropriately normed (SCAN) semilocal density functional.[45] This is because GGA poorly predicts the d-spacing at the high vacancy limit due to the reduction of the coupling between Ca and O, resulting in inaccurate energies of cation migration barrier.[46]

The bond-valence site energy (BVSE) calculations were performed to get insight into the migration path of Ca-ion using the SoftBV package.[47,48] The Ca-ion site energies, $E_{\text{BVSE}}(\text{Ca})$, were calculated for grid points with a resolution of 0.1 Å using the Morse type SoftBV potential. The Ca-ion diffusion pathway is described as the isosurface of constant low $E_{\text{BVSE}}(\text{Ca})$.

The stochastic Ca-ion hopping events in the $Ca_{0.5}Co_2O_4$ were sampled by *ab initio* molecular dynamics (AIMD) simulations with a lower plane-wave cutoff energy of 400 eV and a non-spin polarized setting at the level of GGA exchange–correlation functional. The Γ-point only sampling of k-space was used due to the significant computation effort of AIMD. AIMD simulations were performed at 700, 900, 1200, 1400 K with a time step of 2 fs. Performing AIMD at 1400 K does not result in melting, in agreement with absence of liquid phase up to 1623 K in the experimental Ca–Co–O phase diagram.[49] The supercell of $3 \times 3 \times 1$ replication of the unit cell was fully relaxed at 0 K and heated to 1400 K by velocity scaling at a rate of 140 K ps^{-1}. Then, the supercell was quenched to the desired temperatures at a rate of 140 K ps^{-1} to speed up equilibration at target temperature with respect to Ca ordering and mutual orientation of CoO_2 layers and then equilibrated for 10 ps before measuring the diffusivity. At the desired temperature, AIMD simulations in the NVT ensemble were performed with a Nose–Hoover thermostat[50,51] until the reasonable Einstein relation between mean square displacement (MSD) and time is achieved (>150 ps). The MSD and the diffusivity (D) of Ca atom over time (t) was evaluated by

$$\text{MSD} = \frac{1}{N} \sum_{i=1}^{N} |\mathbf{r}_i(t + t_0) - \mathbf{r}_i(t_0)|^2$$

$$D = \lim_{t \to \infty} \frac{1}{2dt} \text{MSD}$$

where, N is the number of Ca atom, t_0 is the initial time, $\mathbf{r}_i$ is the position vector of individual Ca atom, d is the dimensionality of the system. The activation energy of Ca-ion hopping and the extrapolated diffusivity at the low temperature were obtained from fits to the Arrhenius equation.

Results

Crystal structures of layered calcium cobaltites

The monoclinic $CaCo_2O_4$ simulation cell was prepared by relaxing the structure of Ca-substituted $Na_{0.5}CoO_2$ cell with $C2/m$ symmetry.[52] There are two possible Ca-ion sites and two structures with either of the sites occupied are fully relaxed using DFT calculations at GGA + U level. The DFT energies of both structures are higher than the $P1$ structure by 86 meV per atom because the distance of the first Ca–Ca neighbors in the $C2/m$ structure is shorter (2.95 Å) than that in the $P1$ structure (3.45 Å), inducing strong repulsive interactions (Fig. S2(a) and (b)†). When the $C2/m$ unit cell is doubled in y direction and the Ca atoms alternately occupy the possible Ca-ion sites to mimic the Ca–Ca distance in the $P1$ structure, the result is a similar Ca distribution (3.46 Å) to that in the $P1$ structure and the DFT energy differs only by 1 meV per atom (Fig. S2(c)†). The final structure has the space group of $P2_1/m$ which is similar to that reported in ref. 2 and we use this structure as a ground state of the monoclinic phase.

The two different structures of layered $CaCo_2O_4$ with space group of $P1$ and $P2_1/m$ are shown in Fig. 1(a) and (b), respectively. The edge-sharing Co–O octahedra are connected into CoO_2 layers, and the Ca atoms are intercalated into the interspacing between the layers. In both structures, the Ca atoms are coordinated by O atoms prismatically and the three distinctive stackings of CoO_2 layers are replicated in a periodic fashion,
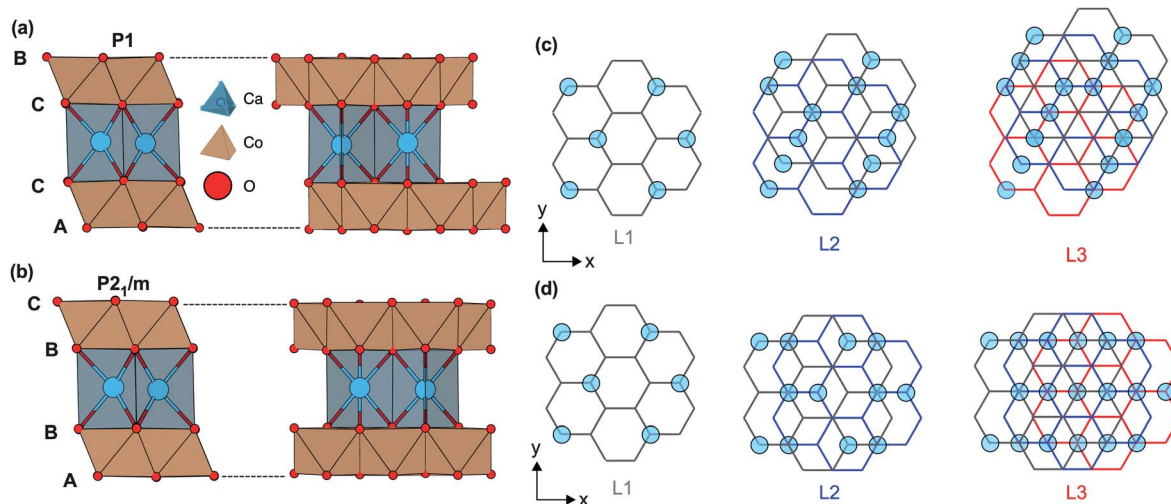

Fig. 1 The crystal structures of P3-type (a) triclinic $P1$ and (b) monoclinic $P2_1/m$ layered $CaCo_2O_4$ shown at two different orientations perpendicular to each other. Blue and red spheres represent Ca and O atoms, respectively. Brown polyhedra are CoO_6 octahedra. The two different stacking sequences in $P1$ and $P2_1/m$ structures are illustrated in (c) and (d), respectively.

21702 | *J. Mater. Chem. A*, 2020, **8**, 21700–21710

This journal is © The Royal Society of Chemistry 2020

corresponding to the P3 structure in the nomenclature of layered structures developed by Delmas.[53] Within the three layers, however, they are stacked in different directions in $P1$ and $P2_1/m$ structures.

The schemes of layer pile-up in $P1$ and $P2_1/m$ are illustrated in Fig. 1(c) and (d), respectively. The hexagonal lattice in the figure is drawn by projecting both the lattice positions of O atom at the bottom of the layer and those of the Co atom into the xy-plane and then connecting them. The Ca atoms reside at the vertices of hexagons, otherwise they would have occupied the unphysical position in which the Ca–O bond length is too short ($\sim$1.6 Å). The distribution of Ca atoms on the CoO_2 layer in $P1$ and $P2_1/m$ is identical with the zigzag pattern with the angle of 60° expanding in y-direction and repeated in x-direction. The ref. 1 reported observations of the same Ca-ion patterning in the $P1$ structure, but suggested that another Ca-ion distribution with the zigzag pattern with the angle of 60° exists in the $P1$ structure (Fig. S3†). We have performed the structure relaxation of the $P1$ simulation cell having the Ca-ion zigzag patterning described in Fig. S3† using DFT + U calculations and the structure ended up with the zigzag patterning shown in Fig. 1(c). The instability of zigzag patterning in Fig. S3† was also observed in $P2_1/m$ structure. Due to the spontaneous relaxation to the configuration in Fig. 1(c), we consider this patterning as the only ground state for $P1$ and $P2_1/m$. The same 60° zigzag ordering of cations is also observed in P3-$Na_{0.5}TiS_2$ and P3-$Na_{0.5}CoO_2$.[54,55]

Although both structures are classified to P3-type layered structure, they are piled up in different fashion. In both structures, adjacent layers were shifted by the one side length of the hexagon relative to each other (L1 in Fig. 1(c) and (d)), but the layers in $P1$ moved in a direction 60° from the x-axis (L2 and L3 in Fig. 1(c)), while the layers in $P2_1/m$ moved in a direction parallel to the x-axis (L2 and L3 in Fig. 1(d)). Eventually, the stacking configurations of CoO_2 layers are the same when $P1$ structure is rotated by 120° around the z-axis, but the configurations of Ca layers are distinctive between these two structures.

In the Table 1, the calculated lattice parameters of $CaCo_2O_4$ with $P1$ and $P2_1/m$ space groups are compared with experimentally observed values. The lattice parameters calculated at the GGA + U level of theory agree with experimental values with an error smaller than 1%. In ref. 27, the hexagonal layered $Ca_xCo_2O_4$ was reported when x is 0.35 or 0.27. The monoclinic

distortion of $P2_1/m$ structure is very small in this range ($D = 2a/b\sqrt{3} = 1.001$; hexagonal lattice if $D = 1$), so the distortion of the hexagonal lattice can be neglected.[2]

Thermodynamics of Ca intercalation reactions

Fig. 2(a) depicts the metastable phase diagram of CaO–CoO–O_2 and the equilibrium phase diagram is given in Fig. S4.† In both diagrams, the $P1$-$CaCo_2O_4$, $Ca_{0.5}Co_2O_4$, $P2_1/m$-$Ca_{0.7}Co_2O_4$, and $Ca_{2/3}Co_2O_4$ are the stable compounds while at the equilibrium the CoO_2 stoichiometry prefers rutile structure and, in the metastable phase diagram, the CoO_2 stoichiometry refers to the layered structure. Previous experiments that synthesized the $CaCo_2O_4$, $Ca_{0.5}Co_2O_4$, and $Ca_{0.7}Co_2O_4$ were found to follow the calculated phase diagram results.[27] For $CaCo_2O_4$, the difference in energy between $P1$ and $P2_1/m$ is only 1 meV per atom, indicating that both $P1$ and $P2_1/m$ can be stabilized in this stoichiometry. The orthorhombic structure with space group $Pnma$ $CaCo_2O_4$ is also experimentally synthesized,[56] but its energy above hull calculated from the equilibrium phase diagram is 63 meV per atom. Liu et al. suggested that cubic spinel $CaCo_2O_4$ could be a promising cathode framework with a reasonably high mobility, but its energy above hull is 114 meV per atom in this study, implying that the layered structure is the ground state of $CaCo_2O_4$. In the charged state, CoO_2, there is no energy difference between $P1$ and $P2_1/m$ since the stacking of CoO_2 layers are the same in both structures as presented in Fig. 1. Noteworthy observation from the phase diagram is that multiple intermediate Ca-ion compositions are stable, suggesting that they can serve as buffer compositions during Ca-ion intercalation preventing the transformation of layered structure. For example, any metastable composition of $Ca_xCo_2O_4$, where x is in the range from 0.7 to 1, will form a mixture of $Ca_{0.7}Co_2O_4$ and $CaCo_2O_4$, not of other types of calcium cobaltite, constraining the reactions to the topotactic interactions.

To fully explore the topotactic reaction space between layered $CaCo_2O_4$ and Co_2O_4, the metastable phase diagram is calculated and presented in Fig. 2(a) on the assumption that the transformation of the layered CoO_2 to the rutile structure is kinetically inhibited. The assumption is based on the small energy above hull of layered CoO_2, which is 13 meV per atom, indicating the thermodynamic driving force to transform into the rutile is relatively small and the transformation can be limited kinetically. From experimentally reported examples of the metastable deintercalated Li cathodes having relatively small energy above hull; layered-CoO_2, olivine-$FePO_4$ ($E_{hull} = 26$ meV), and spinel Mn_2O_4 ($E_{hull} = 32$ meV),[57–59] we can expect the chemically stable layered-CoO_2 upon Ca-ion deintercalation. The magenta line in the metastable phase diagram represents the topotactic Ca-ion intercalation reactions between $P1$-$CaCo_2O_4$ and layered-CoO_2. The additional ground state composition was identified at $P1$-$Ca_{0.25}Co_2O_4$, and the similar composition has been also synthesized previously by ionic exchange of $Na_{0.6}Co_2O_4$.[29]

The arrangements of Ca ions in each layer interact with each other resulting additional stabilization of the overall

Table 1 Lattice parameters of $CaCo_2O_4$ with $P1$ and $P2_1/m$ space groups calculated by GGA + U and observed experimentally

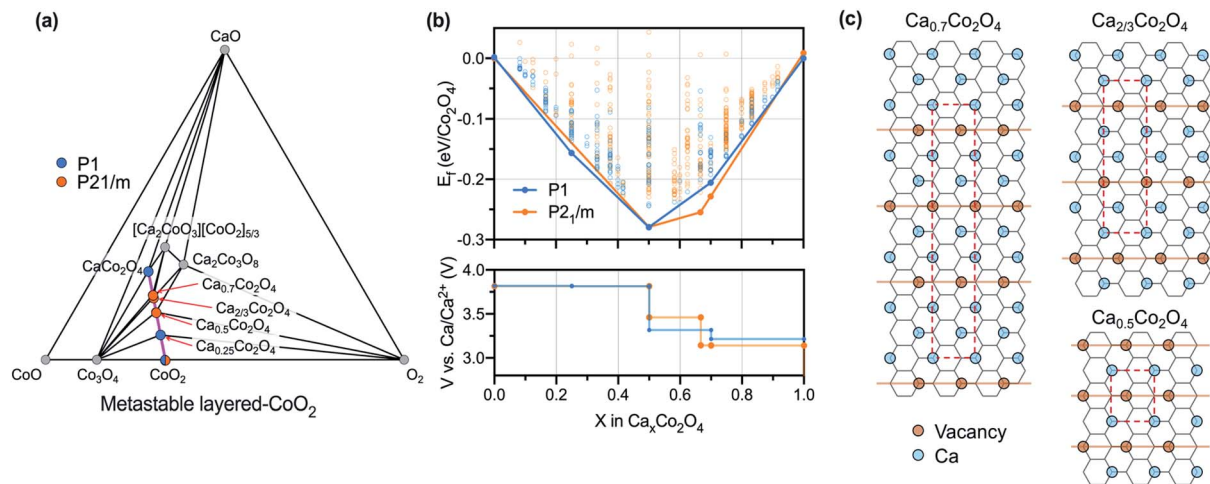|	$P1$		$P2_1/m$	
	GGA + U	Exp[1]	GGA + U	Exp[2]
a (Å)	4.94	4.92	4.95	4.91
b (Å)	5.71	5.68	5.70	5.66
c (Å)	5.68	5.69	5.64	5.62
α (°)	75.4	75.4	90.0	90.0
β (°)	89.9	90.0	106.0	106.1
γ (°)	80.9	81.3	90.0	90.0

Fig. 2 (a) The metastable phase diagram showing stable compounds along the topotactic Ca intercalating reaction (magenta line) between stable $P1$-$CaCo_2O_4$ and metastable layered-CoO_2. (b) The formation energies and convex hulls of $P1$ (blue) and $P2_1/m$ (orange) structures, with metastable compounds delineated by open circles and the ground states by closed circles. The convex hulls are drawn by connecting the ground states at each composition. The corresponding voltage curves of $P1$ and $P2_1/m$ are given at the bottom. (c) The vacancy ordering of $P1$- and $P2_1/m$-$Ca_xCo_2O_4$ at $x = 0.5, 2/3, 0.7$ in which the deepest ground states appear in both cases.
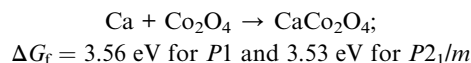
arrangement. To quantitatively compare the stability between $P1$ and $P2_1/m$ structures, which are different in their Ca-ion interlayer interactions, the calculated formation energies and convex hulls of $P1$- and $P2_1/m$-$CaCo_2O_4$ are shown at the top of Fig. 2(b). The calculated convex hulls also enable to determine the corresponding voltage curves, which are drawn at the bottom of Fig. 2(b). Although the ground state convex hull is clearly dominated by that of $P2_1/m$ structures above $x = 0.5$, the distance between two hulls is very close (*e.g.* at $x = 0.7$, 4 meV per atom; at $x = 2/3$, 7 meV per atom; at $x = 0.5$, 0.2 meV per atom; and $x = 0.25$, -7 meV per atom), making a mixture of $P1$ and $P2_1/m$ likely.

During charging of the $P1$ structure, the voltage profile in Fig. 2(b) displays a relatively smooth plateau until extraction Ca to $X = 0.5$, but a large voltage upturn of 0.5 V occurs at $X = 0.5$, drawing two major plateaus. In case of $P2_1/m$, large voltage jumps of 0.32 V and 0.35 V occur at $X = 2/3$ and 0.5, respectively. The magnitude of voltage jumps is loosely related to the depth of the ground state at the convex hull and the emergence of large voltage step signifies the formation of the stable vacancy ordering. The form of stable ordering at a certain composition hinders the further insertion or extraction of intercalants, limiting the maximum electrochemical performance.[60] From this point of view, the extraction of Ca-ion from $P1$ and $P2_1/m$ could be limited to 0.5 Ca and 0.33 Ca per formula unit, respectively. The thermodynamic barriers due to the stable vacancy ordering are commonly observed in layered-$LiCoO_2$.[61] The destabilization of the stable vacancy ordering by thermal or kinetical means can alleviate issues of high thermodynamic barrier, resulting in further Ca utilization.[60]
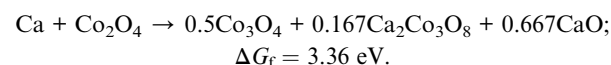
Structures with stable vacancy ordering that are on the hull ($x = 0.7, 2/3$, and 0.5) are illustrated in Fig. 2(c). In all configurations, lines drawn by connecting the vacant Ca-ion sites are aligned perpendicularly to the zigzag pattern of Ca-ion

distribution. At $x = 0.7$ and 2/3, the vacancy orderings in $P1$ and $P2_1/m$ are the same, but their energies show a sizeable difference which is enough to change the shape of the convex hull. In contrast, at $x = 0.5$, both structures show the same vacancy orderings and total energies. The difference between these two observations is to differences in the arrangement of calcium atoms among different Ca-ion layers.

Probing whether the reaction chemistry we are interested in results in the cation insertion or the chemical conversion is crucial in searching for a new intercalation type cathode. The preference between the intercalation and conversion reactions can be ascertained from comparison of the Gibbs free energy of each reaction.[62] The intercalation reaction and the most favorable conversion reactions corresponding to Ca-discharge in the $P1$ and $P2_1/m$ layered-CoO_2 compound can be summarized as

Intercalation:

$$Ca + Co_2O_4 \rightarrow CaCo_2O_4;$$
$$\Delta G_f = 3.56 \text{ eV for } P1 \text{ and } 3.53 \text{ eV for } P2_1/m$$

Conversion:

$$Ca + Co_2O_4 \rightarrow 0.5Co_3O_4 + 0.167Ca_2Co_3O_8 + 0.667CaO;$$
$$\Delta G_f = 3.36 \text{ eV}.$$

Here, we approximate the free energy of a reaction by the DFT total energy as the entropic effect is marginal.[63] The free energy of the reaction of Ca-ion intercalation into the layered-CoO_2 is higher than that of competing chemical decomposition. The preference of intercalation reaction appeared regardless of the space group of the layered-$CaCo_2O_4$. This result demonstrates that the Ca-ion intercalation into the layered-CoO_2 is thermodynamically more favorable than chemical conversion,

21704 | *J. Mater. Chem. A*, 2020, **8**, 21700–21710

This journal is © The Royal Society of Chemistry 2020

indicating that this system is a promising Ca-ion intercalating cathode candidate.

Kinetic properties of intercalated Ca ions

To function as a promising cathode material, the fast-ionic motion is required to enable the topotactic cation intercalating reactions. However, it is expected to be more challenging to be achieved for a multivalent system compared to a monovalent system because of the stronger interaction between cathode frameworks and the moving ions. Hence, it is crucial to probe whether Ca ion mobility is high enough to allow topotactic reactions.

Within the zigzag patterning in the P3 layered structure, there can be two hopping mechanisms, namely, intra- and inter-zigzag hoppings. As depicted in Fig. 3(a), the migrating Ca-ion is moving along the zigzag pattern in the layer through face-sharing prismatic polyhedra (red triangles), which is called intra-zigzag hopping. Another hopping path is that where Ca-ion is hopping across the zigzag lines through nearby face-sharing prismatic polyhedra (red triangles), namely, inter-zigzag hopping as shown at Fig. 3(d).

Calculated minimum energy pathways (MEPs) associated with the migration of Ca-ion through inter-zigzag path at the dilute vacancy concentration limit are illustrated in blue in Fig. 3(f). The Ca-ion migration barriers at dilute vacancy limit are calculated as 0.36 eV and 0.42 eV for $P1$ and $P2_1/m$ structures, respectively. These are the lowest activation energies of

Ca-ion migration ever reported for the stable inorganic compounds containing Ca. Among the calculated Ca migration barriers for experimentally reported inorganic compounds containing Ca, the barrier of 0.72 eV calculated by DFT based NEB at the dilute vacancy limit in $Ca_4Fe_9O_{17}$ was the lowest.[64] The Chevrel phase of $CaMo_6S_8$ was likewise calculated to have a low migration barrier of 0.8 eV.[65,66] The Ca-ion migration barrier is lower in $P1$ structure than $P2_1/m$ by 0.06 eV, which corresponds to an order of magnitude faster diffusivity. In contrast, the intra-zigzag migration mechanism as illustrated in blue in Fig. 3(c) shows the activation energies of 0.72 eV and 0.82 eV in $P1$ and $P2_1/m$ structures, respectively, indicating that the migration of Ca-ion through inter-zigzag networks is energetically favorable in the dilute vacancy limit.

The Ca-ion migration path schematic and MEP at the high-concentration vacancy limit, which is represented by a single Ca-ion migrating in the empty CoO_2 are illustrated in Fig. 4. At the high-concentration vacancy limit, the Ca-ion migration barriers in $P1$ and $P2_1/m$ structures are 0.27 eV and 0.25 eV, respectively. The fast cation motion at the high vacancy concentration refers to the easy insertion of cation to onset the discharging process. To further validate the low activation energies, we have checked whether the low Ca-ion migration energy might be attributed to the fact that the GGA method poorly describes the van der Waals interactions, resulting in a larger interlayer spacing and corresponding low migration barrier in vacancy-rich environment. To remedy this error and
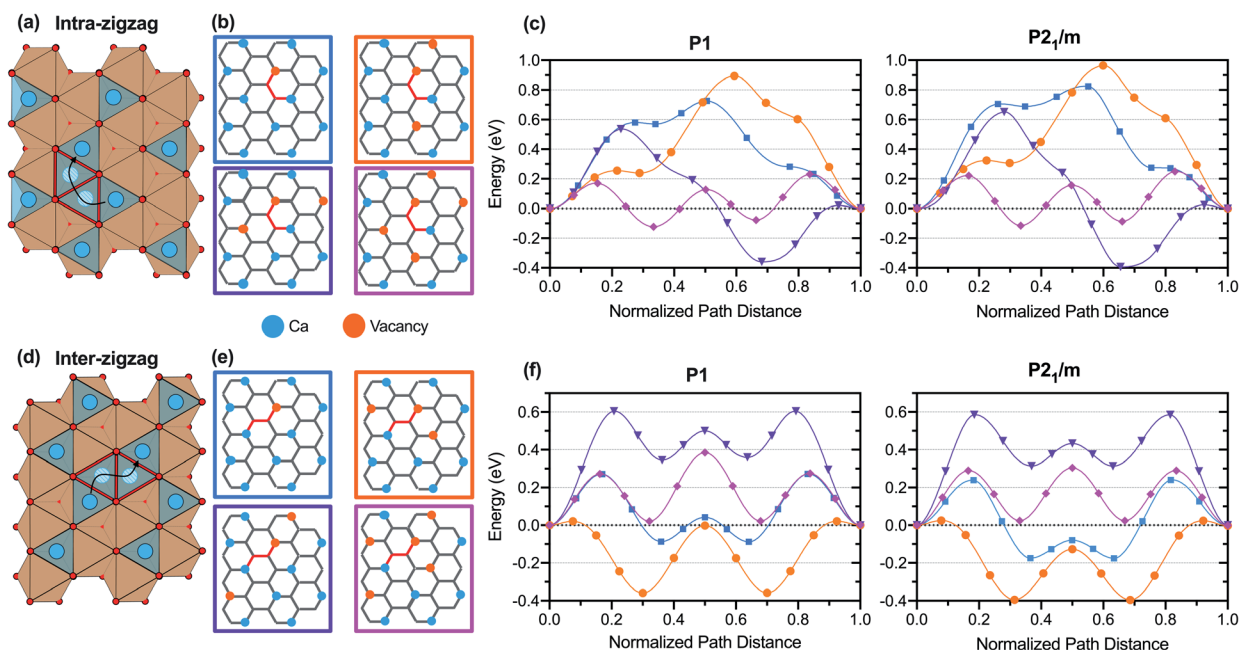

Fig. 3 The schematics of intra- and inter-zigzag migration of Ca within the CoO_2 layer are depicted in (a) and (d). The red triangle represents the prismatic coordination of Ca atoms in the transition states. The local vacancy environments of migrating Ca ions within the layer for intra- and inter-zigzag migrations are illustrated in (b) and (e), respectively. The orange and blue circles represent the vacancies and Ca-ion occupied sites, respectively. The red line follows the Ca-ion migration path. The migration scheme in the blue rectangle represents the migration at the dilute vacancy limit. The migration paths at various local environments of diffusing atom with additional Ca vacancies of either of the two nearest Ca sites to the initial and final states (orange and purple box) or of both of them (magenta box) are also considered. The minimum energy pathways (MEP) for Ca-ion migration in $P1$ and $P2_1/m$ structures for the intra- and inter-zigzag migrations are shown in (c) and (f), respectively. The coloring convention of MEP follows that of the rectangle enclosing the schematics of the local vacancy environments in (b) and (e).
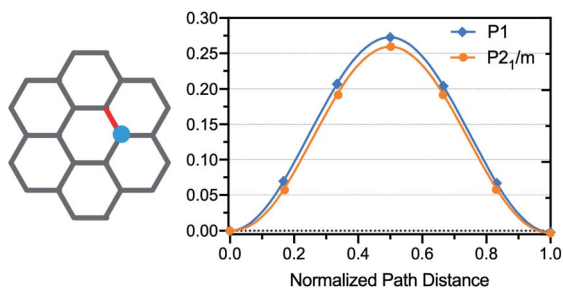
Fig. 4 The path and the MEP of Ca-ion migration in the high-concentration vacancy limit in $P1$ and $P2_1/m$ structures. Blue circle and red line represent the Ca atoms and the diffusion path, respectively.

validate the results, we adopted SCAN semilocal density functional[45] which is a level of meta-GGA method. Although the spacing among CoO_2 layers reduces with SCAN method (5.40 Å → 4.88 Å), the migration barrier does not sensitively respond to the variation of the interspacing distance (Fig. S5†) and remains lower than 0.32 eV.

To fully understand the migration mechanisms, the Ca-ion migration paths at various local vacancy environments are considered. The migration paths with additional Ca-ion vacancy sites adjacent to the diffusing Ca-ion are elaborated in the orange, purple, and magenta boxes in Fig. 3(b) for intra- and (e) for inter-zigzag hopping mechanisms, respectively. For intra-zigzag mechanism, the diffusing Ca ion has only one Ca nearest neighboring at both the initial/final states and at the transition states, respectively, and we considered the various local vacancy environments that result from elimination of the nearest neighbor at either of the initial/final states (orange box in Fig. 3(b)) or at the transition state (purple box in Fig. 3(b)), or both of them (magenta box in Fig. 3(b)). For inter-zigzag mechanism, the diffusing Ca ion has two Ca nearest neighbors at each of the initial and final states, and we considered the various local vacancy environments by removing either of the nearest neighbors (orange and purple boxes in Fig. 3(e)) or both of them (magenta box in Fig. 3(e)). The corresponding MEPs for $P1$ and $P2_1/m$ are plotted in Fig. 3(c) and (f) and the color scheme of MEP follows that of boxes illustrating the local vacancy environments in Fig. 3(b) and (e). Table S1† summarizes migration barriers which are the difference between the minima and maxima in the MEPs.

For intra-zigzag hopping mechanism, removing of the nearest neighbor Ca-ion at either of the initial/final states or the transition state (orange and purple boxes in Fig. 3(b)) results in increase of the Ca-ion migration barriers in both $P1$ and $P2_1/m$ structures within 0.15 eV. Upon removal of all the nearest neighboring Ca atoms (magenta box in Fig. 3(b)), the migration barriers significantly decrease in both structures, to around 0.36 eV. This is attributed to the reduction in the short-range interaction between the diffusing Ca ion and its Ca neighbors due to the absence of the nearest neighboring Ca atoms along the diffusion path. Still, the migration barrier for the intra-zigzag hopping mechanism is generally higher than 0.80 eV and is not particularly sensitive to the variation of the local vacancy environments unless all the nearest neighboring Ca

atoms are removed to reduce the interactions with neighboring Ca atoms.

The inter-zigzag hopping mechanism maintains the trend of low hopping barriers in various vacancy configurations. The local vacancy environments described in the orange and magenta boxes in Fig. 3(e) change the migration barrier only within 0.1 eV in both $P1$ and $P2_1/m$ structures, resulting in the migration barrier that remains lower than 0.42 eV. For the local vacancy structure drawn in the purple box in the Fig. 3(c), however, the Ca-ion migration barriers in $P1$ and $P2_1/m$ increase to about 0.60 eV. Liu et al. suggested that, for 100 nm sized particles, the migration barrier of 0.65 eV is satisfactory for cathode materials in practical charging and discharging conditions,[25] indicating the Ca-ion migration barriers of 0.60 eV in the layered $CaCo_2O_4$ through the inter-zigzag hopping are still acceptable.

The NEB calculations have shown that the Ca-ion migration barriers are dependent on the local atomic environments of diffusing atoms, indicating that large variations in the potential energy landscape complicates determination of the kinetic properties from the single ionic motion. The sensitivity of diffusion barriers to local environments becomes more complex at a higher vacancy concentration because of the manifold of possible vacancy orderings.

To analyse kinetic properties beyond single Ca ion motion, we stochastically sample Ca hopping events using both AIMD and BVSE methods. At Fig. 5(a), for $P1$-$Ca_{0.5}Co_2O_4$ structure, the Ca diffusion pathway as the isosurface of constant low bond valence site energy, $E_{BVSE}(Ca)$, is superimposed on the crystal structure. The Ca atoms migrate along the two-dimensional hexagonal sublattice, which coincides with that shown in Fig. 1(c). Similar Ca migration paths are observed in $P2_1/m$-$Ca_{0.5}Co_2O_4$, $P1$-$CaCo_2O_4$, and $P2_1/m$-$CaCo_2O_4$ (Fig. S6†). The reason for this observed similarity is the analogy of the Ca atom coordination in these structures. If Ca were to approach the center of the hexagon, the number of O neighbors would decrease to only two oxygen atoms, although at a short distance (~1.6 Å). This would reduce strong coulombic interactions with other neighboring oxygen ions, inducing a large energy penalty and, consequently, Ca atoms prefer to diffuse along the edges of the hexagonal-like sublattice. The BVSE calculations suggest that the 2D diffusion network exists at the interlayer between CoO_2 layers in both $P1$ and $P2_1/m$ structures. The diffusion pathway of hexagonal network was confirmed from the AIMD. Fig. 5(b) depicts the diffusion pathways of Ca ions in the $P1$-$Ca_{0.5}Co_2O_4$ structure calculated by AIMD. The Ca-ion migrates along the hexagonal sublattice that corresponds to that predicted by the BVSE method.

Fig. 5(c) shows the Arrhenius plots of diffusivity and the corresponding activation energies of Ca-ion in the $P1$- and $P2_1/m$-$Ca_{0.5}Co_2O_4$ structures. At high temperatures, 1400 K and 1200 K, the mean squared displacements (MSD) of Ca atoms (Fig. S7(a)†) are higher in $P2_1/m$ structure than $P1$, but the order reverses at lower temperatures, 900 K and 700 K (Fig. S7(b)†). The Ca-ion migration barriers calculated from the Arrhenius plots are 0.19 eV and 0.32 eV in $P1$ and $P2_1/m$ structures, respectively. The Ca-ion migration barriers are sufficiently low
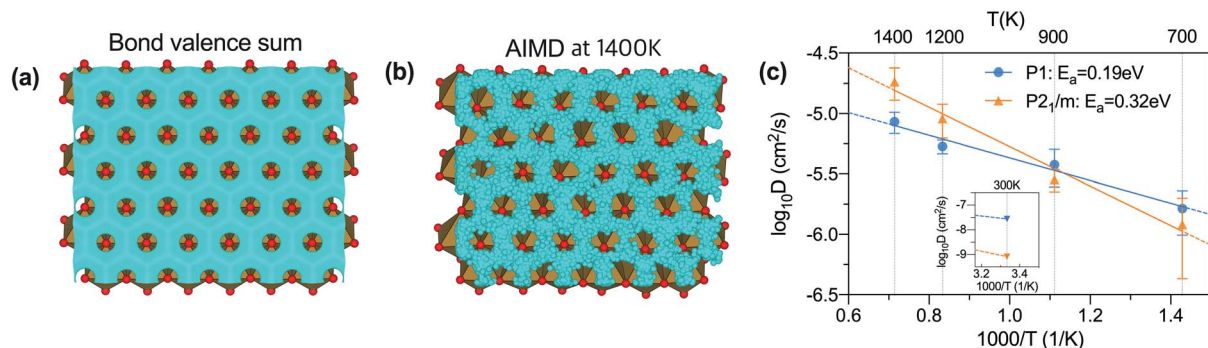
21706 | J. Mater. Chem. A, 2020, 8, 21700–21710

This journal is © The Royal Society of Chemistry 2020

Fig. 5 (a) The Ca diffusion path as the isosurface of constant low bond-valence site energy of Ca within the $P1$-$Ca_{0.5}Co_2O_4$ structure. (b) The Ca diffusion trajectory in the $P1$-$Ca_{0.5}Co_2O_4$ structure calculated by the AIMD at 1400 K. (c) Calculated Arrhenius plots and activation energies for Ca translational diffusion within $P1$-$Ca_{0.5}Co_2O_4$ (blue) and $P2_1/m$-$Ca_{0.5}Co_2O_4$ (orange) structures. The diffusivity at 300 K shown in the inset is extrapolated from the high-temperature data.

in both structures for potential use as cathode materials and, for $P1$ structure, are comparable to activation energies for cathode materials with the high-rate capability. The diffusivity at 300 K extrapolated from the high-temperature data is shown at the inset of Fig. 5(c). The Ca-ion diffusivity in the $P1$ and $P2_1/m$ structure are 3×10^{-8} cm^2 s^{-1} and 8×10^{-10} cm^2 s^{-1}, respectively. Given that typical Li electrode has the Li diffusivity of the order of 10^{-10} to 10^{-6} cm^2 s^{-1} at 400 K, the Ca-ion diffusivity in the CoO_2 interlayers is sufficient to function as electrode materials.[61,63]

Discussion

The trend of fast Ca diffusion in the P3-type layered structure is not found in the other type of layered structure, O3-type, in which Ca atoms are octahedrally coordinated.[67] In P3-type structure, Ca atoms are prismatically coordinated not only at the lattice sites, but also at the migrating intermediate sites as depicted in Fig. 6(a). The Ca atom hops to the symmetry equivalent vacancy sites through the two face-sharing prismatic coordination sites. In the O3-type structure, however, the Ca atom migrates to the adjacent site through a face-sharing

tetrahedra site (Fig. 6(b)) and the Ca migration barriers at the dilute and high vacancy limits are about 0.75 eV which is approximately twice those in P3 structure.[67]

The Ca diffusion barrier is loosely related to the coordination environment along the transition path. Ca prefers high coordination environment in oxides according to Pauling's rules, with preferred coordination number of six or higher.[68] Therefore, the prismatic site with coordination of six is more energetically favorable than a tetrahedral site. As a consequence, the pathway in P3 type structure that proceeds through the centers of polyhedra with the same coordination of six, has a flatter energy profile than the pathway through tetrahedral site in the O3 type structure, resulting in a lower diffusion barrier. Interestingly, the more stable structure also has a lower diffusion barrier, which is opposite to the trend observed previously in calculations on Ca diffusion in V_2O_5 layered structures.[69] There, the stability of the structure was inversely correlated to the diffusion barrier. In our case, the effect of unfavorable intermediate state outweighs the contribution from the initial site stability.

Our results show that preventing transition from the P-type structure to the O-type structure during topotactic
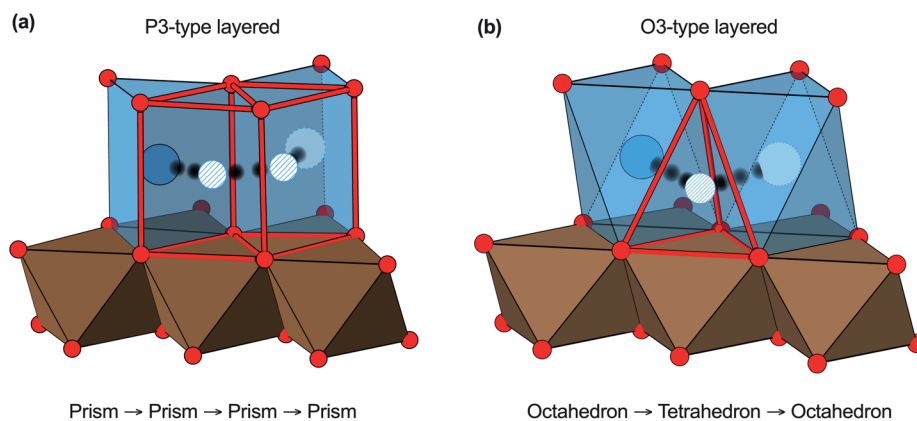

Fig. 6 The Ca diffusion paths in the (a) P3-type and (b) O3-type layered structures. The coordination geometries of Ca at the intermediate diffusing sites are delineated by polyhedrons shaped in red lines. The blue, red spheres, and brown polyhedrons represent the Ca, O, and Co atoms, respectively. The hatched and dashed spheres describe the intermediate and the final sites of diffusing Ca.

This journal is © The Royal Society of Chemistry 2020

J. Mater. Chem. A, 2020, **8**, 21700–21710 | **21707**

intercalation reaction is crucial for the facile Ca ionic motion in the layered CoO_2. In the Na inserted CoO_2, the transition between P- and O-type structures while varying the Na content is observed,[27,70–72] raising a question if a similar behavior occurs in the calcinated CoO_2 and the formation of O-type structure potentially retards the Ca diffusion. However, to the best of our knowledge, the Ca inserted CoO_2 maintains the P-type structure at the Ca content X lower than 1 on $Ca_xCo_2O_4$.[27,29] Note that although Cushing et al.[27] started from $O3$-$NaCoO_2$ for the Na–Ca ionic exchange, the layered $CaCo_2O_4$ formed P-type layered structure, indicating strong driving force to form P-type stacking when calcinated. To assess the difference in stability between P3- and $O3$-$Ca_xCo_2O_4$ at the deintercalated states, we compare the calculated formation energies[67] of partially Ca deintercalated $O3$-$Ca_xCo_2O_4$ with the convex hulls of P3 layered structures (Fig. S8†). The formation energies of O3-type layered structures are higher than those of P3-type structures over the all considered Ca concentrations, indicating that P3-stacking is thermodynamically favorable at partially deintercalated states.

Also, our AIMD simulations ascertain the fast Ca diffusion through the face-sharing prismatic sites at the low Ca content. Overall, the fast Ca diffusion through the prismatic coordination environments is expected in the P-type layered $CaCo_2O_4$ and the partially decalcinated compounds.

Conclusion

We performed first-principles calculations on the layered-$CaCo_2O_4$ and assessed its properties as a cathode material for reversible Ca-ion batteries. Our calculations suggest that thermodynamic and kinetic properties of the layered-$CaCo_2O_4$ make it suitable for use in Ca intercalating cathode.

The desirable cathode materials for intercalation batteries are thermodynamically stable at the various concentration of intercalant, which is calculated in the P3-type layered $CaCo_2O_4$ during the topotactic (de)intercalation of Ca-ion. The layered $Ca_xCo_2O_4$ ($x = 0.5$, 2/3, 0.7, and 1) structures with space groups either $P1$ or $P2_1/m$ are calculated to be thermodynamically stable in the equilibrium phase diagram. Additionally, $Ca_{0.25}Co_2O_4$ is stable in relation to metastable layered CoO_2. Also, the intercalation reaction is energetically more favorable upon insertion of Ca than the conversion reaction.

Along with thermodynamic stability, the CoO_2 framework allows the fast diffusion of Ca along the CoO_2 interlayer spacing. The single ion migration barrier at the high and dilute vacancy concentration limits are as low as 0.36 eV and 0.25 eV, respectively, which are the lowest values reported in the stable inorganic compounds containing Ca. Although varying the Ca vacancy environment of the diffusing atom alters migration energies to some extent, they remain smaller than 0.6 eV when Ca hops by inter-zigzag mechanism. The stochastic sampling of Ca migration events was performed by AIMD, and Ca activation energies were calculated to be 0.19 eV and 0.32 eV for $P1$ and $P2_1/m$ structures, respectively. The diffusivity at room temperature extrapolated using Arrhenius equation is comparable to that of the conventional Li cathode.

The fast diffusion of Ca in the P-type CoO_2 results from the energetically favorable coordination environments of Ca along the transition paths. In the P-type layered structure, as Ca coordination number of six is retained at the intermediate state, Ca atoms diffuse in the smooth energy landscape without a significant energy penalty caused by the unfavorable coordination environments. In O-type CoO_2, in contrast, Ca atoms diffuse through low coordination environments which require a substantial change in the energy along the migration path. Together with the previous experimental observations that the P-type oxygen stackings are kept in the partially Ca deintercalated $CaCo_2O_4$, our results promise the cathode framework for the fast Ca diffusion over the intercalation reaction space. As the P3 stacking is responsible for the fast diffusion of Ca in layered $Ca_xCo_2O_4$, substituting other transition metals for Co in the P3 layered structure and exploring its properties will provide a comprehensive guideline for layered materials as Ca cathodes.

Conflicts of interest

There are no conflicts to declare.

Acknowledgements

References

1 Y. Miyazaki, X. Huang, T. Kajiwara, H. Yamane and T. Kajitani, *J. Ceram. Soc. Jpn.*, 2009, **117**, 42–46.

2 M. Cabello, F. Nacimiento, J. R. González, G. Ortiz, R. Alcántara, P. Lavela, C. Pérez-Vicente and J. L. Tirado, *Electrochem. Commun.*, 2016, **67**, 59–64.

3 M. E. Arroyo-de Dompablo, A. Ponrouch, P. Johansson and M. R. Palacín, *Chem. Rev.*, 2020, **120**(14), 6331–6357.

4 P. Canepa, G. Sai Gautam, D. C. Hannah, R. Malik, M. Liu, K. G. Gallagher, K. A. Persson and G. Ceder, *Chem. Rev.*, 2017, **117**, 4287–4341.

5 A. Ponrouch and M. R. Palacin, *Curr. Opin. Electrochem.*, 2018, **9**, 1–7.

6 P. Vanýsek, in *CRC Handbook of Chemistry and Physics*, ed. J. Rumble, 100th edn, CRC Press LLC, 2019.

7 R. Shannon, *Acta Crystallogr., Sect. A: Cryst. Phys., Diffr., Theor. Gen. Crystallogr.*, 1976, **32**, 751–767.

8 J. Muldoon, C. B. Bucur and T. Gregory, *Chem. Rev.*, 2014, **114**, 11683–11720.

9 R. Y. Wang, C. D. Wessells, R. A. Huggins and Y. Cui, *Nano Lett.*, 2013, **13**, 5748–5752.

10 A. L. Lipson, B. Pan, S. H. Lapidus, C. Liao, J. T. Vaughey and B. J. Ingram, *Chem. Mater.*, 2015, **27**, 8442–8447.

21708 | *J. Mater. Chem. A*, 2020, **8**, 21700–21710

This journal is © The Royal Society of Chemistry 2020

11 T. N. Vo, H. Kim, J. Hur, W. Choi and I. T. Kim, *J. Mater. Chem. A*, 2018, **6**, 22645–22654.

12 M. S. Chae, H. H. Kwak and S.-T. Hong, *ACS Appl. Energy Mater.*, 2020, **3**, 5107–5112.

13 D. Wang, X. Gao, Y. Chen, L. Jin, C. Kuss and P. G. Bruce, *Nat. Mater.*, 2018, **17**, 16.

14 M. Wang, C. Jiang, S. Zhang, X. Song, Y. Tang and H.-M. Cheng, *Nat. Chem.*, 2018, **10**, 667–672.

15 Z. Li, O. Fuhr, M. Fichtner and Z. Zhao-Karger, *Energy Environ. Sci.*, 2019, **12**, 3496–3501.

16 A. Shyamsunder, L. E. Blanc, A. Assoud and L. F. Nazar, *ACS Energy Lett.*, 2019, **4**, 2271–2276.

17 S. J. Richard Prabakar, A. B. Ikhe, W. B. Park, K.-C. Chung, H. Park, K.-J. Kim, D. Ahn, J. S. Kwak, K.-S. Sohn and M. Pyo, *Adv. Sci.*, 2019, **6**, 1902129.

18 J. Park, Z.-L. Xu, G. Yoon, S. K. Park, J. Wang, H. Hyun, H. Park, J. Lim, Y.-J. Ko, Y. S. Yun and K. Kang, *Adv. Mater.*, 2020, **32**, 1904411.

19 K. Mizushima, P. C. Jones, P. J. Wiseman and J. B. Goodenough, *Mater. Res. Bull.*, 1980, **15**, 783–789.

20 R. Berthelot, D. Carlier and C. Delmas, *Nat. Mater.*, 2011, **10**, 74–80.

21 J.-J. Braconnier, C. Delmas, C. Fouassier and P. Hagenmuller, *Mater. Res. Bull.*, 1980, **15**, 1797–1804.

22 Y. Hironaka, K. Kubota and S. Komaba, *Chem. Commun.*, 2017, **53**, 3693–3696.

23 L. W. Shacklette, *J. Electrochem. Soc.*, 1988, **135**, 2669.

24 S. Yagi, Y. Ichikawa, I. Yamada, T. Doi, T. Ichitsubo and E. Matsubara, *Jpn. J. Appl. Phys.*, 2013, **52**, 025501.

25 M. Liu, Z. Rong, R. Malik, P. Canepa, A. Jain, G. Ceder and K. A. Persson, *Energy Environ. Sci.*, 2015, **8**, 964–974.

26 N. Sa, A. Mukherjee, B. Han, Y. Ren, R. F. Klie, B. Key and J. T. Vaughey, *J. Power Sources*, 2019, **424**, 68–75.

27 B. L. Cushing and J. B. Wiley, *J. Solid State Chem.*, 1998, **141**, 385–391.

28 T. Kanno, S. Yotsuhashi and H. Adachi, *Appl. Phys. Lett.*, 2004, **85**, 739–741.

29 H. X. Yang, Y. G. Shi, X. Liu, R. J. Xiao, H. F. Tian and J. Q. Li, *Phys. Rev. B: Condens. Matter Mater. Phys.*, 2006, **73**, 014109.

30 P. Hohenberg and W. Kohn, *Phys. Rev.*, 1964, **136**, B864–B871.

31 G. Kresse and J. Furthmuller, *Phys. Rev. B: Condens. Matter Mater. Phys.*, 1996, **54**, 11169–11186.

32 P. E. Blöchl, *Phys. Rev. B: Condens. Matter Mater. Phys.*, 1994, **50**, 17953–17979.

33 G. Kresse and D. Joubert, *Phys. Rev. B: Condens. Matter Mater. Phys.*, 1999, **59**, 1758–1775.

34 J. P. Perdew, K. Burke and M. Ernzerhof, *Phys. Rev. Lett.*, 1996, **77**, 3865–3868.

35 S. L. Dudarev, G. A. Botton, S. Y. Savrasov, C. J. Humphreys and A. P. Sutton, *Phys. Rev. B: Condens. Matter Mater. Phys.*, 1998, **57**, 1505–1509.

36 A. Jain, G. Hautier, S. P. Ong, C. J. Moore, C. C. Fischer, K. A. Persson and G. Ceder, *Phys. Rev. B: Condens. Matter Mater. Phys.*, 2011, **84**, 045115.

37 V. L. Chevrier, S. P. Ong, R. Armiento, M. K. Y. Chan and G. Ceder, *Phys. Rev. B: Condens. Matter Mater. Phys.*, 2010, **82**, 075122.

38 S. P. Ong, W. D. Richards, A. Jain, G. Hautier, M. Kocher, S. Cholia, D. Gunter, V. L. Chevrier, K. A. Persson and G. Ceder, *Comput. Mater. Sci.*, 2013, **68**, 314–319.

39 A. Van der Ven, J. C. Thomas, Q. Xu and J. Bhattacharya, *Math. Comput. Simulat.*, 2010, **80**, 1393–1410.

40 G. Henkelman, B. P. Uberuaga and H. Jónsson, *J. Chem. Phys.*, 2000, **113**, 9901–9904.

41 G. K. P. Dathar, D. Sheppard, K. J. Stevenson and G. Henkelman, *Chem. Mater.*, 2011, **23**, 4032–4037.

42 S. P. Ong, V. L. Chevrier, G. Hautier, A. Jain, C. Moore, S. Kim, X. Ma and G. Ceder, *Energy Environ. Sci.*, 2011, **4**, 3680–3688.

43 H. Lin, Y. Wen, C. Zhang, L. Zhang, Y. Huang, B. Shan and R. Chen, *Solid State Commun.*, 2012, **152**, 999–1003.

44 T. Eom, H.-K. Lim, W. A. Goddard and H. Kim, *J. Phys. Chem. C*, 2015, **119**, 556–562.

45 J. Sun, A. Ruzsinszky and J. P. Perdew, *Phys. Rev. Lett.*, 2015, **115**, 036402.

46 K. Kang, Y. S. Meng, J. Bréger, C. P. Grey and G. Ceder, *Science*, 2006, **311**, 977.

47 H. Chen and S. Adams, *IUCrJ*, 2017, **4**, 614–625.

48 H. Chen, L. L. Wong and S. Adams, *Acta Crystallogr., Sect. B: Struct. Sci., Cryst. Eng. Mater.*, 2019, **75**, 18–33.

49 D. Sedmidubský, V. Jakeš, O. Jankovský, J. Leitner, Z. Sofer and J. Hejtmánek, *J. Solid State Chem.*, 2012, **194**, 199–205.

50 W. G. Hoover, *Phys. Rev. A*, 1985, **31**, 1695–1697.

51 S. Nosé, *J. Chem. Phys.*, 1984, **81**, 511–519.

52 Y. Ono, R. Ishikawa, Y. Miyazaki, Y. Ishii, Y. Morii and T. Kajitani, *J. Solid State Chem.*, 2002, **166**, 177–181.

53 C. Delmas, J.-J. Braconnier, C. Fouassier and P. Hagenmuller, *Solid State Ionics*, 1981, **3–4**, 165–169.

54 J. Vinckevičiūtė, M. D. Radin and A. Van der Ven, *Chem. Mater.*, 2016, **28**, 8640–8650.

55 J. L. Kaufman and A. Van der Ven, *Phys. Rev. Mater.*, 2019, **3**, 015402.

56 M. Shizuya, M. Isobe and E. Takayama-Muromachi, *J. Solid State Chem.*, 2007, **180**, 2550–2557.

57 A. Jain, G. Hautier, C. J. Moore, S. Ping Ong, C. C. Fischer, T. Mueller, K. A. Persson and G. Ceder, *Comput. Mater. Sci.*, 2011, **50**, 2295–2310.

58 A. Jain, S. P. Ong, G. Hautier, W. Chen, W. D. Richards, S. Dacek, S. Cholia, D. Gunter, D. Skinner, G. Ceder and K. A. Persson, *APL Mater.*, 2013, **1**, 011002.

59 K. Shimoda, M. Murakami, D. Takamatsu, H. Arai, Y. Uchimoto and Z. Ogumi, *Electrochim. Acta*, 2013, **108**, 343–349.

60 T. Chen, G. Sai Gautam, W. Huang and G. Ceder, *Chem. Mater.*, 2018, **30**, 153–162.

61 A. Van der Ven and G. Ceder, *J. Power Sources*, 2001, **97–98**, 529–531.

62 D. C. Hannah, G. Sai Gautam, P. Canepa and G. Ceder, *Adv. Energy Mater.*, 2018, **8**, 1800379.

63 A. Urban, D.-H. Seo and G. Ceder, *npj Comput. Mater.*, 2016, **2**, 16002.

This journal is © The Royal Society of Chemistry 2020

J. Mater. Chem. A, 2020, **8**, 21700–21710 | **21709**

64 A. P. Black, A. Torres, C. Frontera, M. R. Palacín and M. E. Arroyo-de Dompablo, *Dalton Trans.*, 2020, **49**, 2671–2679.

65 C. Geantet, J. Padiou, O. Peña, M. Sergent and R. Horyn, *Solid State Commun.*, 1987, **64**, 1363–1368.

66 M. Smeu, M. S. Hossain, Z. Wang, V. Timoshevskii, K. H. Bevan and K. Zaghib, *J. Power Sources*, 2016, **306**, 431–436.

67 H. Park, Y. Cui, S. Kim, J. T. Vaughey and P. Zapol, *J. Phys. Chem. C*, 2020, **124**, 5902–5909.

68 I. D. Brown, *Acta Crystallogr., Sect. B: Struct. Sci.*, 1988, **44**, 545–553.

69 G. S. Gautam, P. Canepa, R. Malik, M. Liu, K. Persson and G. Ceder, *Chem. Commun.*, 2015, **51**, 13619–13622.

70 Q. Huang, M. L. Foo, R. A. Pascal, J. W. Lynn, B. H. Toby, T. He, H. W. Zandbergen and R. J. Cava, *Phys. Rev. B: Condens. Matter Mater. Phys.*, 2004, **70**, 184110.

71 L. Viciu, J. W. G. Bos, H. W. Zandbergen, Q. Huang, M. L. Foo, S. Ishiwata, A. P. Ramirez, M. Lee, N. P. Ong and R. J. Cava, *Phys. Rev. B: Condens. Matter Mater. Phys.*, 2006, **73**, 174104.

72 Y. Lei, X. Li, L. Liu and G. Ceder, *Chem. Mater.*, 2014, **26**, 5288–5296.

73 B. Jeon, J. W. Heo, J. Hyoung, H. H. Kwak, D. M. Lee and S.-T. Hong, *Chem. Mater.*, 2020, DOI: 10.1021/acs.chemmater.0c01112.

74 S. Kim, L. Yin, M. H. Lee, P. Parajuli, L. Blanc, T. T. Fister, H. Park, B. J. Kwon, B. J. Ingram, P. Zapol, R. F. Klie, K. Kang, L. F. Nazar, S. H. Lapidus and J. T. Vaughey, *ACS Energy Lett.*, 2020, 3203–3211.